

1 Formation of the energetic electrons at the dipolarization front and the trailing flux pileup region 2 during magnetic reconnection

3 JIA NAN ,^{1,2} QUANMING LU ,^{1,2} KAI HUANG ,³ SAN LU ,^{1,2} RONGSHENG WANG ,^{1,2} AND SHIHANG HU ,^{1,2}

4 ¹*School of Earth and Space Sciences/Deep Space Exploration Laboratory, University of Science and Technology of China, Hefei 230026, China*

5 ²*Collaborative Innovation Center of Astronautical Science and Technology, Harbin, China*

6 ³*School of Physics, Harbin Institute of Technology, Harbin, 150001, China*

ABSTRACT

8 The dipolarization front (DF) and the flux pileup region (FPR) are crucial downstream structures
9 in magnetic reconnection, where significant energetic electrons are frequently observed. Using a two-
10 dimensional particle-in-cell simulation model, we investigate the formation of energetic electrons in both
11 the DF and the trailing FPR. Our results demonstrate that the energetic electrons at pitch angles near
12 90° at both regions undergo a two-stage acceleration process: an initial non-adiabatic acceleration by
13 the reconnection electric field at the reconnection site followed by downstream adiabatic acceleration.
14 We find that the 90° pitch-angle energetic electrons in the FPR reach substantially higher energies
15 than those at the DF, as they encounter a stronger reconnection electric field at the reconnection site
16 in the first stage. Furthermore, two populations of energetic electrons with distinct energy ranges at
17 pitch angles near 0° and 180° are identified at the DF. The lower-energy population exhibits energies
18 close to the magnitude of the parallel potential at the DF, which dominates the formation of this
19 population by accelerating the electrons towards the DF and providing the trapping mechanism. The
20 higher-energy population is energized via Fermi mechanism through multiple reflections within the
21 contracting magnetic island downstream. These findings provide new insights into the generation of
22 energetic electrons during magnetic reconnection.

23 *Keywords:* space plasmas (1544) — plasma physics (2089) — planetary magnetospheres (997)

24 1. INTRODUCTION

25 Magnetic reconnection is a fundamental physical process in plasma for energy conversion from magnetic energy
26 into particle kinetic energy, and it drives explosive phenomena in space, astrophysical, and laboratory plasmas (R.
27 Giovanelli 1946; P. Sweet 1958; A. Nishida & S.-I. Akasofu 1979; R. McPherron 1987; S. Tsuneta et al. 1992; J. Lin
28 & T. Forbes 2000; V. Angelopoulos et al. 2008; M. Yamada et al. 2010; T. Zhang et al. 2012; Y.-H. Liu et al. 2017;
29 Y. Shu et al. 2021; Q. Lu et al. 2022, 2025; R. Wang et al. 2023; L. Dai et al. 2024; S. Wang et al. 2024; F. Yang
30 et al. 2025; K. Huang et al. 2025a,b). Magnetic reconnection features a multi-scale diffusion region characterized by
31 a small electron diffusion region (EDR) embedded within a more extensive ion diffusion region (IDR) (J. Birn & M.
32 Hesse 2001; P. Pritchett 2001; F. Mozer et al. 2002; T. Nagai et al. 2003; Q. Lu et al. 2010; A. Divin et al. 2012).
33 Furthermore, magnetic reconnection generates crucial downstream signatures, including the flux pileup region (FPR)
34 (M. Hesse & J. Birn 1991; H. Zhang et al. 2007; M. Wu et al. 2015; C. Liu et al. 2017) and dipolarization front (DF)
35 (V. Angelopoulos et al. 1992; M. Ashour-Abdalla et al. 2011; H. Fu et al. 2013; S. Lu et al. 2015, 2016).

36 The FPR forms where magnetic flux accumulates as a high-speed reconnection outflow decelerates upon colliding
37 with the pre-existing plasma sheet (M. Hoshino et al. 2001; C. Liu et al. 2020). The leading edge of this propagating
38 structure is known as the DF, characterized by a sharp increase in the magnetic field component normal to the neutral
39 sheet (M. Sitnov et al. 2009; M. Wu et al. 2013; Y. Shu et al. 2021; M. Oka et al. 2023), which is also called the
40 reconnection front. The DFs and their trailing FPRs are frequently detected by in-situ spacecraft measurements in

41 the Earth's magnetotail plasma sheet (R. Nakamura et al. 2002; M. Sitnov et al. 2009; A. Runov et al. 2009; M. Wu
 42 et al. 2013; C. Liu et al. 2017), and the significant enhancements in energetic electron flux are observed within these
 43 regions (J. Birn et al. 2014; V. Angelopoulos et al. 2013; M. Zhou et al. 2013; S. Huang et al. 2015; H. Fu et al. 2019;
 44 X. Xing et al. 2024).

45 The generation mechanism of energetic electrons at the DF and FPR has drawn significant attention in recent years.
 46 Within these structures, electrons can gain perpendicular energy through betatron acceleration, as they encounter the
 47 enhanced magnetic field of the piling magnetic flux (H. S. Fu et al. 2011; J. Birn et al. 2013; C. Huang et al. 2015;
 48 K. Huang et al. 2021; Y. Yu et al. 2023). They can also undergo Fermi acceleration, gaining parallel energy through
 49 repeated reflections along contracting magnetic field lines in the outflow region (X. R. Fu et al. 2006; J. Drake et al.
 50 2006; S. Lu et al. 2016; C. Liu et al. 2017; Q. Lu et al. 2018; K. Huang et al. 2021). The parallel electric field is also found
 51 to be important to provide the trapping mechanism, enabling continuous and efficient betatron acceleration at the DF
 52 (C. Huang et al. 2015). In addition to those downstream processes, the electron acceleration at the reconnection site
 53 (near the X-line) is another vital process for the generation of energetic electrons, as evidenced by numerous simulations
 54 and in-situ observations (M. Øieroset et al. 2002; X. R. Fu et al. 2006; R. Wang et al. 2010a,b; C. Huang et al. 2010;
 55 S. Huang et al. 2012). The existence of these distinct acceleration processes suggests that electrons may go through a
 56 multi-stage acceleration process. M. Hoshino et al. (2001) proposed that electrons are primarily accelerated
 57 by the reconnection electric field near the X-line, and subsequently undergo further energization via
 58 gradient and curvature drift motion within the FPR. Observational works in the Earth's magnetotail
 59 also suggest that electrons can experience a multi-stage acceleration process (M. Wu et al. 2015; Y.
 60 Xu et al. 2018). Meanwhile, energetic electrons with diverse pitch angle distributions are frequently
 61 observed in these two regions (H. S. Fu et al. 2011; M. Wu et al. 2013; C. Liu et al. 2017). However,
 62 the specific connection between the different energization processes and the role of those processes in
 63 the formation of energetic electrons at different pitch angles observed at the FPR/DF, remain unclear.
 64

65 In this work, by utilizing a two-dimensional particle-in-cell (PIC) simulation, we study the formation of energetic
 66 electrons in the DF and its trailing FPR during magnetic reconnection. In our results, the energetic electrons in the
 67 FPR are predominantly concentrated at pitch angles near 90°, whereas those at the DF are observed at pitch angles
 68 near 0°, 90°, and 180°. We find that the 90° pitch-angle energetic electrons in both regions undergo a two-stage
 69 acceleration process, in which electrons are initially accelerated at the reconnection site by the reconnection electric
 70 field, then transported downstream where they undergo further adiabatic acceleration. Furthermore, we identify two
 71 populations of energetic electrons with distinct energy ranges at pitch angles near 0° and 180°, and demonstrate their
 72 different formation mechanisms.

73 2. SIMULATION MODEL

74 This study is conducted by performing a two-dimensional (2-D) particle-in-cell (PIC) simulation, and the software
 75 used in this paper has been successfully validated in our previous works on magnetic reconnection and plasma waves
 76 (X. R. Fu et al. 2006; Q. Lu et al. 2010; C. Chang et al. 2021; J. Nan et al. 2022). The simulation domain is in the
 77 x-z plane. A Harris current sheet with no guide field is given as the initial configuration:

$$78 \mathbf{B} = B_0 \tanh(z/\delta) \mathbf{e}_x \quad (1)$$

$$79 \quad 80 n = n_0 \operatorname{sech}^2(z/\delta) + n_b \quad (2)$$

81 , where B_0 represents the asymptotic magnitude of the magnetic field, δ represents the half-thickness of the current
 82 sheet, n_0 and n_b represent the peak density of current sheet and the background density, respectively. Here, we use
 83 $n_b = 0.05n_0$ and $\delta = 0.75d_i$, where d_i is the ion inertial length based on n_0 . Two plasma species, electrons and ions,
 84 are used in the simulation. The reduced mass ratio is set to be $m_i/m_e = 100$. The initial velocity distributions of
 85 the two species are Maxwellian with temperature ratio $T_i/T_e = 4$, and the temperature of the current sheet plasma is
 86 4 times that of the background plasma. The speed of light is set to be $c/V_A = 15$, where $V_A = B_0/\sqrt{n_0 m_i \mu_0}$ is the
 87 Alfvén speed, and the upstream Alfvén speed is defined as $V_{Ab} = B_0/\sqrt{n_b m_i \mu_0}$ based on background plasma density.

88 The simulation box is $L_x \times L_z = 100d_i \times 40d_i$. The spatial resolution is $\Delta x = \Delta z = 0.025d_i$. The time step
 89 adopted to push the simulation forward is $\Delta t = 0.001\Omega_i^{-1}$, where $\Omega_i = eB_0/m_i$ is the ion gyro-frequency. In the
 90 z direction, perfect conducting boundaries are used for electromagnetic field, and reflecting boundaries are used for

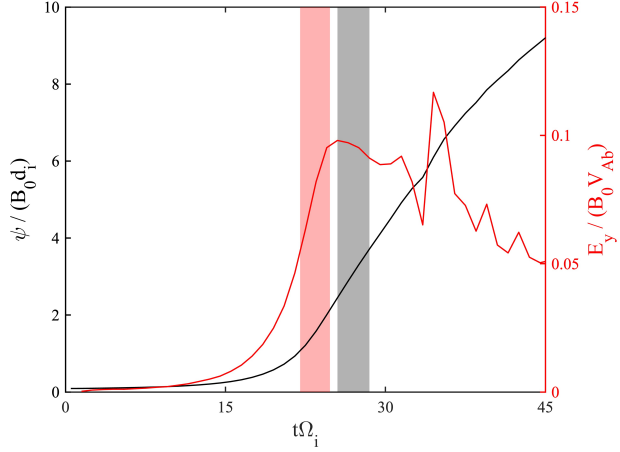


Figure 1. Time evolution of the magnetic flux ψ (black line) and the reconnection electric field E_y (red line) at the X-line. The red and grey shaded regions represent the time intervals $t\Omega_i = 22 - 24.8$ and $t\Omega_i = 25.5 - 28.5$, during which the retraced electrons originating from the DF and FPR (denoted in the white boxes in Figure 3(b1)-(b2)) travel through the reconnection site, correspondingly.

91 particles. Periodic boundaries are used in the x direction. A total of 1×10^9 pseudo particles of each species are
 92 used in the simulation. In order to trigger the reconnection, we impose an initial perturbation of magnetic flux on the
 93 equilibrium state in the form of $\psi_1 = 0.1B_0d_i \operatorname{sech}^2(x/2\delta) \operatorname{sech}^2(z/\delta)$.

3. RESULTS

94 Figure 1 shows the evolution of the magnetic flux ψ and the reconnection electric field E_y at the X-line. The
 95 magnetic reconnection starts quickly at approximately $t\Omega_i = 15$ under the trigger of the imposed initial perturbation.
 96 The reconnection electric field E_y at the X-line reaches its first peak of about $0.1B_0V_{Ab}$ at around $t\Omega_i = 25.5$, which
 97 is consistent with previous results (Y.-H. Liu et al. 2017; J. Nan et al. 2022; Q. Lu et al. 2025). Subsequently,
 98 the reconnection electric field decays slowly although there are some fluctuations, and drops to about $0.05B_0V_{Ab}$ at
 99 $t\Omega_i = 45$.
 100

101 Figure 2 displays the spatial distributions of (a1)-(a2) the magnetic field magnitude B , (b1)-(b2) the parallel potential
 102 $e\phi_{\parallel}$, (c1)-(c2) the electron perpendicular temperature $T_{e\perp}$, (d1)-(d2) the electron parallel temperature
 103 $T_{e\parallel}$, and (e1)-(e2) the temperature ratio $T_{e\perp}/T_{e\parallel}$ at $t\Omega_i = 32$ and 40 , respectively. The definition of the parallel
 104 potential is $e\phi_{\parallel}(x, z) = e \int_{(x, z)}^{\infty} E_{\parallel} dl$, the integration of the work done by parallel electric field on electrons along
 105 the magnetic field lines (J. Egedal et al. 2015; J. Nan et al. 2022). The two time slots are selected to describe the
 106 development of the DF and FPR. We identify the DF as the region centered around the magnetic field maximum along
 107 the $z = 0$ and spanning approximately one ion inertial length ($\sim 1d_i$) in extent. The trailing region of the DF is the
 108 FPR, which is distinguished as the region where $(\partial B / \partial t + V_{flux,x} \partial B / \partial x) > 0$ is satisfied in the downstream of the EDR,
 109 where $V_{flux,x}$ is the propagation speed of the magnetic flux in the x direction calculated by tracing the same magnetic
 110 flux along the $z = 0$. The DF and FPR ranges along the $z = 0$ are shown in Figure 2(f1)-(f2). At $t\Omega_i = 32$, the
 111 early stage of the DF, these two regions exhibit distinct plasma and field characteristics. The magnetic field strength
 112 is significantly enhanced at the DF, reaching approximately $1.5B_0$, while it is comparatively weaker in the trailing
 113 FPR. A strong, localized parallel potential ($e\phi_{\parallel}$) with a magnitude up to $6T_{e0}$ (equivalent to $24T_{eb}$) develops at the
 114 DF, primarily resulting from the charge separation, which has already been studied in previous works (C. Huang et al.
 115 2015; S. Hu et al. 2025). However, the parallel potential in the FPR is substantially weaker. Although both regions
 116 show significant perpendicular heating, the average perpendicular temperature in the FPR (about $5T_{e0}$) is notably
 117 higher than at the DF (about $3T_{e0}$). Conversely, the DF exhibits enhanced parallel temperature, with $T_{e\parallel}$ reaching
 118 around $2T_{e0}$, whereas there is no obvious parallel heating in the FPR. This suggests that the DF possesses a parallel
 119 energization that is absent in the FPR. Consequently, a strong temperature anisotropy of $T_{e\perp}/T_{e\parallel} > 1$ is developed at
 120 the FPR, while the parallel and perpendicular temperature are comparable at the DF at this time. At $t\Omega_i = 40$, the
 121 DF has evolved into a developed state, in which the magnetic field at the DF intensifies further to a magnitude of $2B_0$.
 122 Meanwhile, the parallel potential increases to approximately $8T_{e0}$. Concurrently, the DF exhibits increased parallel

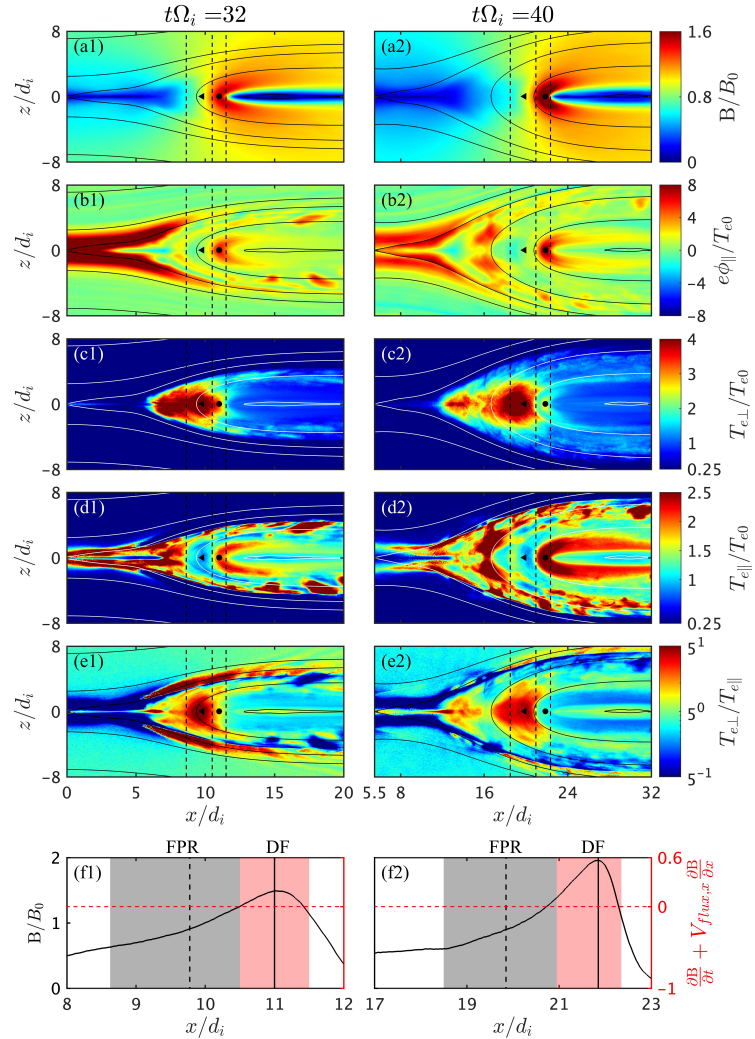


Figure 2. (a1)-(a2) The magnitude of magnetic field B , (b1)-(b2) the parallel potential $e\phi_{\parallel}$, where we define $e\phi_{\parallel}(x, z) = e \int_{(x, z)}^{\infty} E_{\parallel} dl$, the integration of the work done by parallel electric field on electrons from the boundary along the magnetic field lines, (c1)-(c2) the electron perpendicular temperature $T_{e\perp}$, (d1)-(d2) the electron parallel temperature $T_{e\parallel}$, and (e1)-(e2) the temperature ratio $T_{e\perp}/T_{e\parallel}$ at $t\Omega_i = 32$ and 40, respectively. The curves represent the magnetic field lines. Three vertical lines denote the boundaries separating the FPR(left) and the DF(right). (f1)-(f2) $(\frac{\partial B}{\partial t} + V_{flux,x} \frac{\partial B}{\partial x})$ (red lines) and the magnetic field magnitude(black lines) along $z = 0$ plane at $t\Omega_i = 32$ and 40, where $V_{flux,x}$ is the propagation speed of the magnetic flux in the x direction. The shaded regions represent the FPR(grey) and DF(red). Note that the left boundary of the FPR at $t\Omega_i = 32$ is determined by the EDR boundary. Representative locations at the DF and FPR are marked correspondingly by filled triangles and rounds in panels (a1)-(e1) and (a2)-(e2), and vertical lines in panels (f1)-(f2).

123 temperature (around $2.8T_{e0}$) alongside a decrease in the perpendicular temperature (around $2.2T_{e0}$). This leads to the
 124 development of a temperature anisotropy of $T_{e\perp}/T_{e\parallel} < 1$ at the DF, whereas the condition $T_{e\perp}/T_{e\parallel} > 1$ is maintained
 125 in the FPR. Representative locations in each region are selected and marked in Figure 2 for further analysis.

126 **Figure 3** presents the normalized electron velocity distribution $f(v_{e\parallel}, v_{e\perp})$ and the normalized energy
 127 spectrum at different pitch angles $F(\epsilon_e, \theta)$ at representative locations within the FPR and DF at $t\Omega_i = 32$
 128 and 40. The normalization adopted here is $\iint f(v_{e\parallel}, v_{e\perp}) v_{e\perp} dv_{e\perp} dv_{e\parallel} = \iint F(\epsilon_e, \theta) \sin(\theta) d\epsilon_e d\theta = n_e/n_0$,
 129 where n_e is the local electron density. At $t\Omega_i = 32$, energetic electrons in the FPR (Figures 3(a1) and 3(b1))

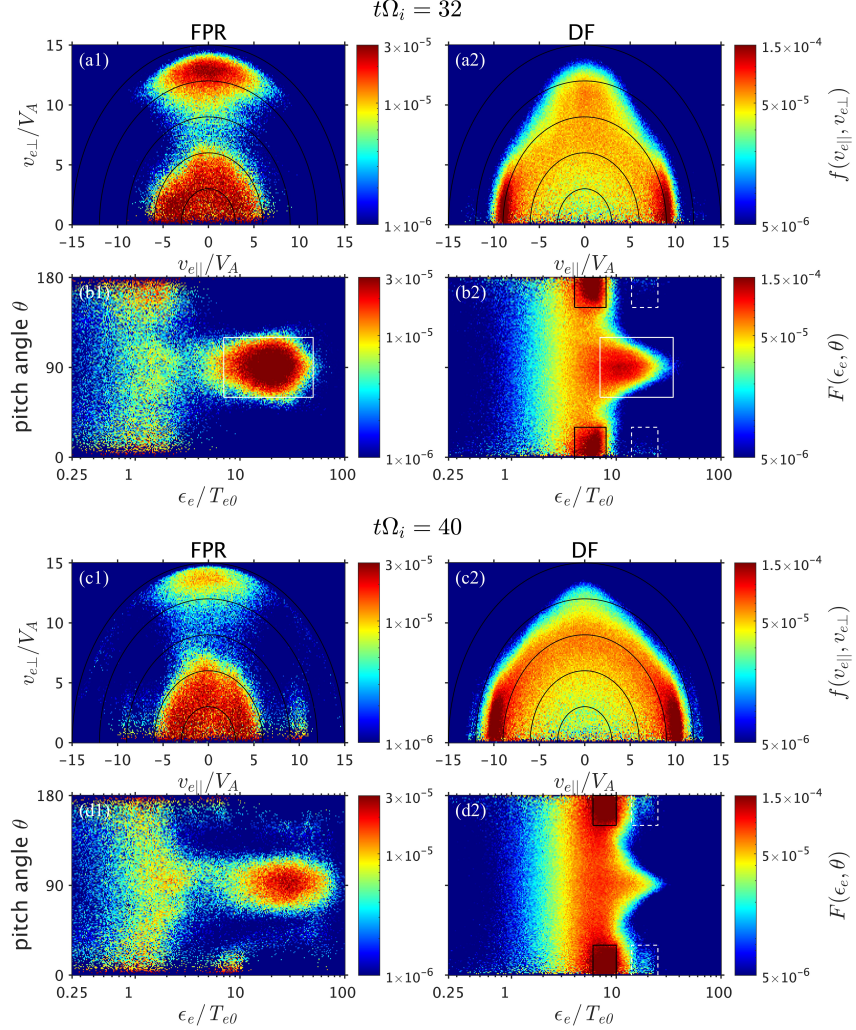


Figure 3. (a1)-(a2) and (c1)-(c2) the normalized velocity distribution of electrons $f(v_{e\parallel}, v_{e\perp})$, (b1)-(b2) and (d1)-(d2) the normalized energy spectrum at different pitch angles $F(\epsilon_e, \theta)$ at the selected locations of DF and FPR at $t\Omega_i = 32$ and 40 (as denoted in Figure 2), where ϵ_e represents electron energy and θ represents the pitch angle. Here $\iint f(v_{e\parallel}, v_{e\perp}) v_{e\perp} dv_{e\perp} dv_{e\parallel} = \iint F(\epsilon_e, \theta) \sin(\theta) d\epsilon_e d\theta = n_e / n_0$, where n_e is the local electron density. The energetic electrons at pitch angles $|\theta - 90^\circ| < 30^\circ$ with energies $7T_{e0} < \epsilon_e < 50T_{e0}$ at the FPR and energies $7T_{e0} < \epsilon_e < 35T_{e0}$ at the DF are denoted by the white boxes in (b1)-(b2) at $t\Omega_i = 32$, respectively. The energetic electrons at pitch angles $|\theta - 90^\circ| > 60^\circ$ with energies $7T_{e0} < \epsilon_e < 50T_{e0}$ at the DF are denoted by black boxes in panel (b2). The energetic electrons at pitch angles $|\theta - 90^\circ| > 60^\circ$ with energies $14T_{e0} < \epsilon_e < 25T_{e0}$ at the DF are denoted by white dashed boxes at the two time slots.

are primarily concentrated at pitch angles near 90° . This population has an averaged energy of about $21T_{e0}$ with a maximum energy reaching up to about $70T_{e0}$ (denoted by the white box in Figure 3(b1)). The remaining population in the FPR **consists of** a nearly isotropic, low-energy thermal component with energies below $3T_{e0}$. At the DF (Figures 3(a2) and 3(b2)), the **distribution of energetic electrons are observed at pitch angles near 0° , 90° , and 180°** . The 90° pitch-angle population (denoted by the white box in Figure 3(b2)) has an average energy of about $12T_{e0}$ with a maximum energy up to approximately $40T_{e0}$, which is considerably lower than that in the FPR. Two populations of energetic electrons with distinct energy ranges are present at pitch angles near 0° and 180° at the DF. The lower-energy population **consists of** electrons with energies in the range of $4-8T_{e0}$ (denoted by black boxes in Figure 3(b2)), close to the magnitude of the parallel potential at the DF ($\sim 6T_{e0}$). It turns out that the parallel potential dominates the formation of this population, which will be displayed in detail later. The higher-energy population spans an energy range of about $14-25T_{e0}$ (denoted by white dashed boxes in Figure 3(b2)), well exceeding the magnitude of the parallel potential. This population is attributed to the Fermi acceleration process (X. R. Fu et al. 2006; K.

Huang et al. 2021), whereby electrons are energized through multiple reflections within the contracting magnetic island formed downstream due to periodic boundaries in the x direction.

We next examine the electron distributions at these two regions at $t\Omega_i = 40$, when the DF is well developed. In the FPR (Figures 3(c1) and (d1)), the electron distribution is still primarily composed of the 90° pitch-angle energetic population and the low-energy thermal population, similar to that at the earlier time. The energies of the high-energy population increase further, but the phase space density of this population is substantially reduced. At the DF (Figures 3(c2) and 3(d2)), a decrease in the energy spectrum of energetic electrons with pitch angles near 90° is observed. This is attributed to particle loss along the magnetic field, driven by the magnetic mirror force originating from the localized magnetic hump at the DF (K. Huang et al. 2021). Meanwhile, the energies of the lower-energy population at pitch angles near 0° and 180° are increased to $6-10T_{e0}$ (denoted by black solid boxes in Figure 3(d2)), corresponding to the intensification of the parallel potential to $\sim 8T_{e0}$. The energy spectrum of the higher-energy population at pitch angles near 0° and 180° is notably enhanced (denoted by white dashed boxes in Figure 3(d2)), consistent with K. Huang et al. (2021) that the contribution from Fermi reflection is more significant in later stage. We have confirmed that the formation of this higher-energy population is due to the Fermi process through particle tracing, but as it has been detailed in the previous works (X. R. Fu et al. 2006; K. Huang et al. 2021), the analysis is not repeated here.

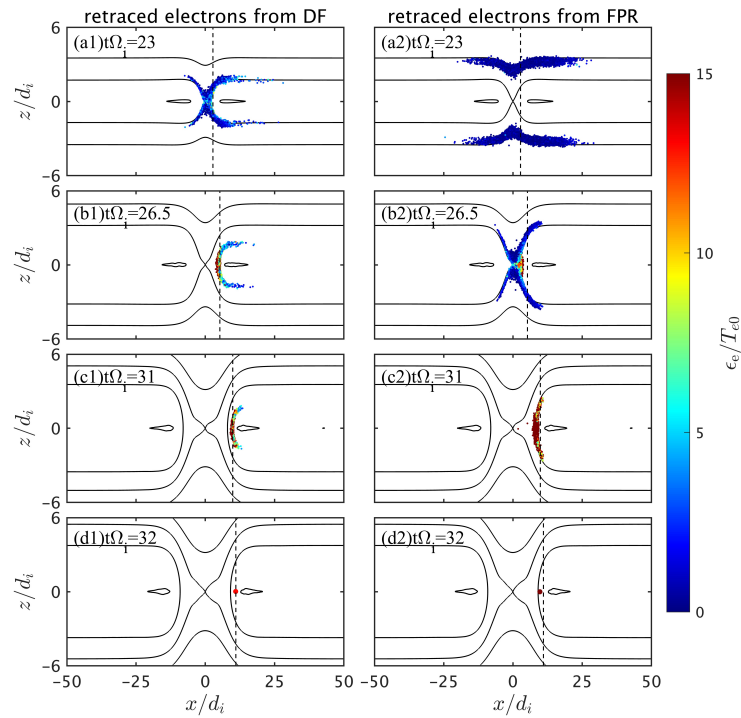


Figure 4. Spatial distributions for the retraced energetic electrons with pitch angles near 90° ($|\theta - 90^\circ| < 30^\circ$) from (a1-d1) the DF and (a2)-(d2) FPR at $\Omega_i t = 23, 26, 31$ and 32 . Those retraced electrons are denoted in white boxes in Figure 3(b1) and 3(b2). The vertical dashed lines mark the location of the maximum of B along $z = 0$ in $x > 0$ domain at each time slot for reference. The colors represent the energies of electrons. The curves represent the magnetic field lines.

To understand the acceleration processes of energetic electrons observed at the DF and FPR, we retrace the trajectories (backward in time) of those electrons selected at $t\Omega_i = 32$, when the flux of 90° pitch-angle energetic electrons at the DF has not decreased. We first describe the formation of the 90° pitch-angle energetic populations at these two regions (denoted in white boxes in Figure 3(b1)-(b2)). Figure 4 shows the spatial distributions of the retraced electrons originating from the DF (a1)-(d1) and FPR (a2)-(d2) at different time slots. Figure 5 shows the time evolution of their averaged (a) magnetic moment μ , (b) electron energy ϵ_e , (c) local magnetic field magnitude B, and (d) $|\theta - 90^\circ|$, where θ is the pitch angle. To simplify the description, we hereafter refer these populations

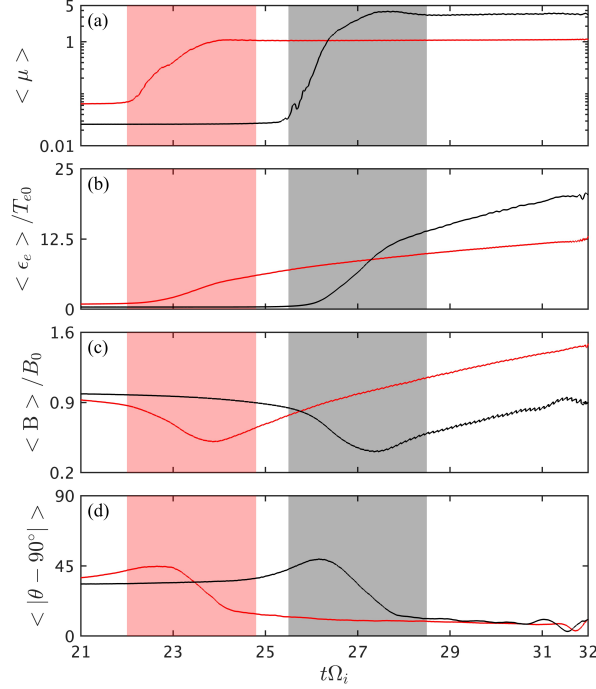


Figure 5. Time evolution of averaged (a) magnetic moment μ , (b) electron energy ϵ_e , (c) local magnetic field B , and (d) $|\theta - 90^\circ|$, where θ is the pitch angle, of the retraced electrons with pitch angles near 90° ($|\theta - 90^\circ| < 30^\circ$) from the DF (red lines) and FPR (black lines) at $t\Omega_i = 32$, respectively. The red and grey shaded regions mark the time intervals during which the averaged magnetic moment of the retraced electrons from the DF and FPR are not conserved, respectively.

as DF electrons and FPR electrons, respectively. Both the DF electrons and FPR electrons experience a two-stage acceleration process, which is an initial non-adiabatic acceleration near the X-line, followed by an adiabatic acceleration in the outflow region. In the first stage, electrons are accelerated by reconnection electric field at the reconnection site, where their magnetic moment is not conserved. The DF electrons undergo this first-stage acceleration at about $t\Omega_i = 22 - 24.8$ (as shown in Figure 4(a1)), gaining an average energy of $5T_{e0}$ (red shaded region in Figure 5). In contrast, the FPR electrons pass through the reconnection site later around $t\Omega_i = 25.5 - 28.5$ (as shown in Figure 4(b2)), when the reconnection electric field is stronger than that experienced by the DF electrons (the time periods are also denoted in Figure 1), allowing FPR electrons to gain a higher energy of $13.4T_{e0}$ on average (grey shaded region in Figure 5). In the second stage, electrons are transported downstream and undergo an adiabatic acceleration due to the magnetic field compression with conserved magnetic moment. **During this stage, the pitch angles of those electrons are very close to 90° (the averaged $|\theta - 90^\circ|$ is less than 15° as shown in Figure 5(d)), which means that the energies of those electrons are mainly allocated in the perpendicular direction.** Therefore, the energization efficiency of individual electrons can be described by:

$$\frac{d\epsilon_e}{dt} = \mu \frac{dB}{dt} = \frac{\epsilon_{e0}}{B_0} \frac{dB}{dt} \quad (3)$$

, where ϵ_{e0} is the electron energy and B_0 is the local magnetic field strength at the beginning of this stage. Integrating Eq.3 yields $\epsilon_e = \epsilon_{e0}B/B_0$, which suggests that the final energy ϵ_e in the second stage depends on two factors: the initial energy ϵ_{e0} and the relative change in magnetic field (B/B_0). Although the DF electrons experience a larger magnetic field amplification ($B/B_0=2.26$ on average) compared to the FPR electrons ($B/B_0=1.52$ on average), their initial energies are significantly lower in this stage ($\epsilon_{e0}= 6.0T_{e0}$ for DF electrons and $\epsilon_{e0}=13.9T_{e0}$ for FPR electrons on average). Ultimately, the electrons arriving at the FPR reach higher final energies ($20.7T_{e0}$ on average) compared with those arriving at the DF ($12.4T_{e0}$ on average).

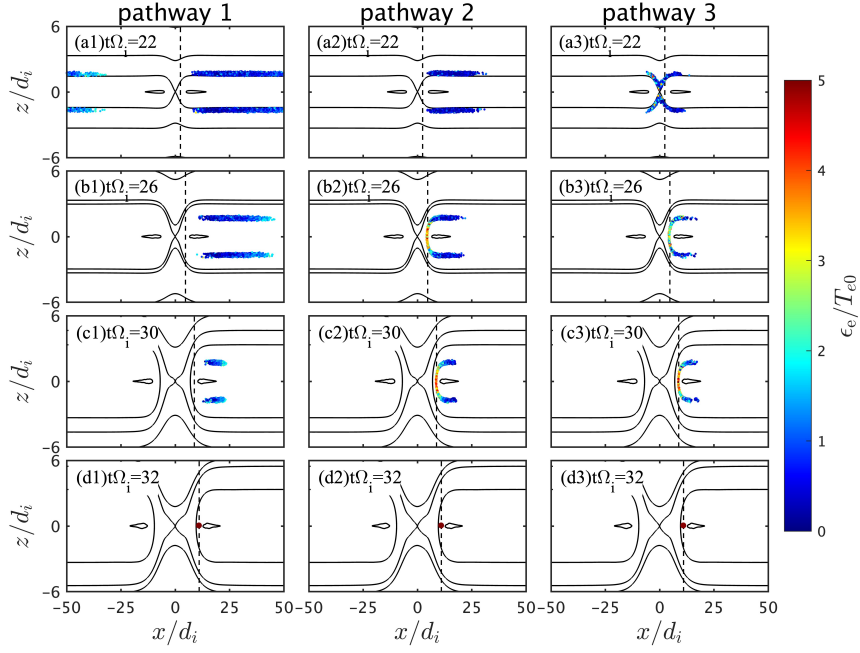


Figure 6. Spatial distributions of the retraced lower-energy population of energetic electrons at pitch angles near 0° and 180° ($|\theta - 90^\circ| > 60^\circ$) at the DF involving in the three pathways at $t\Omega_i = 22, 26, 30$, and 32 , respectively. Those retraced electrons are denoted in black boxes in Figure 3(b2). The vertical dashed lines mark the location of the maximum of B along $z = 0$ in $x > 0$ domain at each time slot for reference. The colors represent the energies of electrons. The curves represent the magnetic field lines.

186 A distinguishing feature of the energetic electron distribution at the DF is the presence of the lower-energy population
 187 at pitch angles near 0° and 180° (denoted by black solid boxes in Figure 3(b2)), which is absent in the FPR. The
 188 formation of this population can be categorized into three pathways, as illustrated by the spatial distributions of
 189 the retraced electrons in Figure 6. Figure 7 quantifies the energization of the population in each pathway, the
 190 contributions from the electric field components using the following equation:

$$191 \Delta\epsilon_e = \int -ev_{||}E_{||}dt + \int -ev_{\perp}\cdot\mathbf{E}_{\perp}dt \quad (4)$$

192 In the first pathway (accounting for 56% of the population), electrons are accelerated towards the DF in a single
 193 pass by the parallel electric field ($E_{||}$) along the magnetic field (Figure 6(a1)-(d1)). In this pathway, $E_{||}$ is the primary
 194 contributor to the total energy gain. In the second pathway (35% of the population), electrons are also drawn towards
 195 the mid-plane by $E_{||}$ but are subsequently trapped, executing a bouncing motion around the mid-plane (Figure 6(a2)-
 196 (d2)). The trapping mechanism is primarily provided by the parallel potential, as the magnetic mirror force is negligible
 197 due to their small magnetic moment. The third pathway (9% of the population) involves electrons that travel through
 198 the reconnection site (Figure 6(a3)). They gain only modest amounts of energy from the reconnection electric field and
 199 are subsequently trapped by parallel potential. In the second and third pathways, the perpendicular electric field (E_{\perp})
 200 primarily contributes the energy gain (Figure 7(b) and 7(c)). However, because the first pathway constitutes more
 201 than half of the population, the total averaged contribution from $E_{||}$ is comparable to that from E_{\perp} (Figure 7(d)).
 202 Given the vital roles of parallel potential in both accelerating electrons towards the DF and providing the trapping
 203 mechanism, we conclude that the parallel potential dominates the formation of this population. These energization
 204 processes also explain why the energies of this population are close to the magnitude of the parallel potential. The
 205 electrons in the first pathway originating upstream are energized by the parallel potential and also mildly accelerated
 206 by E_{\perp} , thus they arrive the DF with energies slightly exceeding the parallel potential. For electrons in the second and
 207 third pathways, their energies are limited by the parallel potential due to the confinement within the potential well.

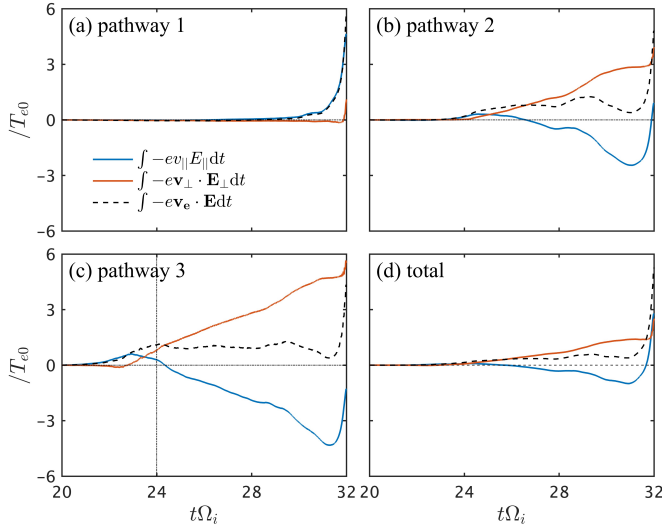


Figure 7. Time integration of the work done by electric field on (a)-(c) electrons involving in the three pathways and (d) the total population, averaging over electrons. The vertical dashed line in panel(c) marks the time when the electrons in the third pathway leaves the reconnection site.

4. CONCLUSIONS AND DISCUSSION

In summary, we investigate the formation of energetic electrons observed at the DF and FPR during magnetic reconnection by performing a 2D PIC simulation. The energetic electrons in the FPR are predominantly concentrated at pitch angles near 90° , whereas those at the DF are observed at pitch angles near 0° , 90° , and 180° . Our results demonstrate that the 90° pitch-angle energetic electrons in the FPR and DF both undergo a two-stage acceleration process. They are initially energized near the X-line by the reconnection electric field and then transported downstream, where they experience further adiabatic acceleration. The energy gain in the first stage is critical in determining the final electron energy. Electrons arriving at the FPR traveling through the reconnection site at a later time, when the reconnection electric field is stronger, granting them significantly greater energization (approximately 2.7 times that of electrons arriving at the DF in the first stage). The efficiency of the second-stage acceleration is determined by two factors: the relative change in magnetic field and the initial electron energy in this stage. Therefore, although electrons arriving at the DF experience a stronger magnetic field compression in the second stage, the insufficient pre-acceleration from the first stage limits the subsequent adiabatic acceleration. As a result, the electrons arriving at the FPR reach substantially higher energies than those arriving at the DF. Concurrently, two populations of energetic electrons with distinct energy ranges at pitch angles near 0° and 180° are identified at the DF. We demonstrate that the lower-energy population exhibits energies close to the magnitude of the parallel potential at the DF. The parallel potential dominates the formation of this population by accelerating the electrons towards the DF and providing the trapping mechanism. Meanwhile, the higher-energy population is energized via the Fermi mechanism through multiple reflections within contracting magnetic islands downstream.

Our findings can be viewed in relation to the pioneering work of [M. Hoshino et al. \(2001\)](#), which suggests that the nonadiabatic motion of electrons in the FPR plays an important role in electron energization. In their study, the employment of a relatively small simulation domain may limit the development of magnetic flux pileup, possibly leading to nonadiabatic motion of electrons around the midplane where the magnetic field remains moderate. The larger simulation domain employed in our work allows the FPR develop further, and the magnetic field around the midplane within the FPR intensifies to the order of the upstream magnetic field. Therefore, adiabatic motion dominates the acceleration process in the FPR in our results.

These simulation results provide a comprehensive interpretation for satellite observations of electron temperature anisotropy at the DF and FPR. Consistent with the observations in ([Y. V. Khotyaintsev et al. 2011](#)), we reproduce

238 the anisotropy of $T_{e\perp}/T_{e\parallel} > 1$ in the FPR and the anisotropy of $T_{e\perp}/T_{e\parallel} < 1$ at the DF in the later stage of reconnection
 239 (around $t\Omega_i = 40$ in our simulation). We propose that the temperature anisotropy in the FPR results from the effective
 240 perpendicular electron energization by the two-stage acceleration. The reversed anisotropy at the DF is attributed to
 241 the combined effect of (1) **the increase of the electron parallel temperature** resulting from both the enhanced
 242 parallel potential and the more sufficient Fermi acceleration, and (2) the reduction of the perpendicular flux due to
 243 particle loss at the DF.

244 Strong parallel potential can also form near the X-line during magnetic reconnection, particularly
 245 under low upstream β_e conditions (J. Egedal et al. 2013). J. Egedal et al. (2013) highlight its con-
 246 tribution to confine the electrons sufficiently long time so that energization at the reconnection site
 247 becomes effective during anti-parallel reconnection. We point out that both the 90° pitch-angle ener-
 248 getic population (the second-stage acceleration) and the lower-energy 0° and 180° population (electrons
 249 involved in the second and third pathways) at the DF share an analogous energization process, which
 250 underscores the importance of the parallel potential in producing energetic electrons during magnetic
 251 reconnection.

252 The earlier studies have investigated the outward-propagating energetic electrons in the outflow
 253 region that appear as part of the Hall current system (M. Øieroset et al. 2001; Q. Lu et al. 2010).
 254 In our results, we identify a significant population of inward-propagating energetic electrons in the
 255 outflow region (electrons in the first pathway shown in Figure 6), as well as a population executing
 256 bounce motion along the magnetic field(electrons in the second and third pathways shown in Figure
 257 6). These populations can also contribute to the Hall current, which reveals a more complex picture
 258 of the Hall reconnection system.

ACKNOWLEDGMENTS

259 This work is supported by the National Key Research and Development Program of China (No. 2022YFA1604600).
 260 The simulation dataset (the electromagnetic field data and particle data used to plot the figures in this
 261 work) can be downloaded from: <https://doi.org/10.57760/sciencedb.30394>.

REFERENCES

262 Angelopoulos, V., Runov, A., Zhou, X.-Z., et al. 2013, *Science*, 341, 1478

263 Angelopoulos, V., Baumjohann, W., Kennel, C. F., et al. 1992, *Journal of Geophysical Research: Space Physics*, 97, 4027, doi: <https://doi.org/10.1029/91JA02701>

264 Angelopoulos, V., McFadden, J. P., Larson, D., et al. 2008, *Science*, 321, 931

265 Ashour-Abdalla, M., El-Alaoui, M., Goldstein, M. L., et al. 2011, *Nature Physics*, 7, 360

266 Birn, J., & Hesse, M. 2001, *Journal of Geophysical Research: Space Physics*, 106, 3737

267 Birn, J., Hesse, M., Nakamura, R., & Zaharia, S. 2013, *Journal of Geophysical Research: Space Physics*, 118, 1960

268 Birn, J., Runov, A., & Hesse, M. 2014, *Journal of Geophysical Research: Space Physics*, 119, 3604

269 Chang, C., Huang, K., Lu, Q., et al. 2021, *Journal of Geophysical Research: Space Physics*, 126, e2021JA029290

270 Dai, L., Zhu, M., Ren, Y., et al. 2024, *Nature Communications*, 15, 639

271 Divin, A., Lapenta, G., Markidis, S., et al. 2012, *Journal of Geophysical Research: Space Physics*, 117, doi: <https://doi.org/10.1029/2011JA017464>

272 Drake, J., Swisdak, M., Che, H., & Shay, M. 2006, *Nature*, 443, 553

273 Egedal, J., Daughton, W., Le, A., & Borg, A. L. 2015, *Physics of Plasmas*, 22

274 Egedal, J., Le, A., & Daughton, W. 2013, *Physics of Plasmas*, 20

275 Fu, H., Khotyaintsev, Y. V., Vaivads, A., Retinò, A., & André, M. 2013, *Nature Physics*, 9, 426

276 Fu, H., Xu, Y., Vaivads, A., & Khotyaintsev, Y. V. 2019, *The Astrophysical Journal Letters*, 870, L22

297 Fu, H. S., Khotyaintsev, Y. V., André, M., & Vaivads, A.
 298 2011, *Geophysical Research Letters*, 38

299 Fu, X. R., Lu, Q. M., & Wang, S. 2006, *Physics of Plasmas*,
 300 13, 012309, doi: [10.1063/1.2164808](https://doi.org/10.1063/1.2164808)

301 Giovanelli, R. 1946, *Nature*, 158, 81

302 Hesse, M., & Birn, J. 1991, *Journal of Geophysical
 303 Research: Space Physics*, 96, 19417

304 Hoshino, M., Mukai, T., Terasawa, T., & Shinohara, I.
 305 2001, *Journal of Geophysical Research: Space Physics*,
 306 106, 25979

307 Hu, S., Lu, Q., Shu, Y., et al. 2025, *The Astrophysical
 308 Journal*, 986, 43

309 Huang, C., Lu, Q., & Wang, S. 2010, *Physics of Plasmas*, 17

310 Huang, C., Wu, M., Lu, Q., Wang, R., & Wang, S. 2015,
 311 *Journal of Geophysical Research: Space Physics*, 120,
 312 1759

313 Huang, K., Ling, W., Tang, H., et al. 2025a, *Physics of
 314 Plasmas*, 32

315 Huang, K., Lu, Q., Lu, S., Wang, R., & Wang, S. 2021,
 316 *Journal of Geophysical Research: Space Physics*, 126,
 317 e2021JA029939

318 Huang, K., Ling, W., Tang, H., et al. 2025b, *Geophysical
 319 Research Letters*, 52, e2025GL117351

320 Huang, S., Vaivads, A., Khotyaintsev, Y. V., et al. 2012,
 321 *Geophysical Research Letters*, 39

322 Huang, S., Fu, H., Yuan, Z., et al. 2015, *Journal of
 323 Geophysical Research: Space Physics*, 120, 4496

324 Khotyaintsev, Y. V., Cully, C., Vaivads, A., André, M., &
 325 Owen, C. 2011, *Physical Review Letters*, 106, 165001

326 Lin, J., & Forbes, T. 2000, *Journal of Geophysical
 327 Research: Space Physics*, 105, 2375

328 Liu, C., Fu, H., Liu, Y., et al. 2020, *Journal of Geophysical
 329 Research: Space Physics*, 125, e2020JA027777

330 Liu, C., Fu, H., Xu, Y., Cao, J., & Liu, W. 2017,
 331 *Geophysical Research Letters*, 44, 6492

332 Liu, Y.-H., Hesse, M., Guo, F., et al. 2017, *Phys. Rev.
 333 Lett.*, 118, 085101, doi: [10.1103/PhysRevLett.118.085101](https://doi.org/10.1103/PhysRevLett.118.085101)

334 Lu, Q., Fu, H., Wang, R., & Lu, S. 2022, *Chinese Physics
 335 B*, 31, 089401

336 Lu, Q., Huang, C., Xie, J., et al. 2010, *Journal of
 337 Geophysical Research: Space Physics*, 115,
 338 doi: <https://doi.org/10.1029/2010JA015713>

339 Lu, Q., Shu, Y., Chang, C., Lu, S., & Wang, R. 2025,
 340 *Science Bulletin*, 70, 2766,
 341 doi: <https://doi.org/10.1016/j.scib.2025.06.014>

342 Lu, Q., Wang, H., Huang, K., Wang, R., & Wang, S. 2018,
 343 *Physics of Plasmas*, 25

344 Lu, S., Angelopoulos, V., & Fu, H. 2016, *Journal of
 345 Geophysical Research: Space Physics*, 121, 9483,
 346 doi: <https://doi.org/10.1002/2016JA022815>

347 Lu, S., Lu, Q., Lin, Y., et al. 2015, *Journal of Geophysical
 348 Research: Space Physics*, 120, 6286

349 McPherron, R. 1987, *Quantitative Modeling of
 350 Magnetosphere-Ionosphere Coupling Processes*, 252

351 Mozer, F., Bale, S., & Phan, T. 2002, *Physical review
 352 letters*, 89, 015002

353 Nagai, T., Shinohara, I., Fujimoto, M., et al. 2003, *Journal
 354 of Geophysical Research: Space Physics*, 108

355 Nakamura, R., Baumjohann, W., Klecker, B., et al. 2002,
 356 *Geophysical research letters*, 29, 3

357 Nan, J., Huang, K., Lu, Q., et al. 2022, *Journal of
 358 Geophysical Research: Space Physics*, 127,
 359 e2021JA029996

360 Nishida, A., & Akasofu, S.-I. 1979, *Geomagnetic Diagnosis
 361 of the Magnetosphere (Physics and Chemistry in Space,
 362 Volume 9)*, American Institute of Physics

363 Øieroset, M., Lin, R., Phan, T., Larson, D., & Bale, S.
 364 2002, *Physical Review Letters*, 89, 195001

365 Øieroset, M., Phan, T., Fujimoto, M., Lin, R., & Lepping,
 366 R. 2001, *Nature*, 412, 414

367 Oka, M., Birn, J., Egedal, J., et al. 2023, *Space Science
 368 Reviews*, 219, 75

369 Pritchett, P. 2001, *Journal of Geophysical Research: Space
 370 Physics*, 106, 3783

371 Runov, A., Angelopoulos, V., Sitnov, M., et al. 2009,
 372 *Geophysical Research Letters*, 36

373 Shu, Y., Lu, S., Lu, Q., Ding, W., & Wang, S. 2021,
 374 *Journal of Geophysical Research: Space Physics*, 126,
 375 e2021JA029712

376 Sitnov, M., Swisdak, M., & Divin, A. 2009, *Journal of
 377 Geophysical Research: Space Physics*, 114

378 Sweet, P. 1958, in *Symposium-International Astronomical
 379 Union*, Vol. 6, Cambridge University Press, 123–134

380 Tsuneta, S., Hara, H., Shimizu, T., et al. 1992, *PASJ:*
 381 *Publications of the Astronomical Society of Japan (ISSN
 382 0004-6264)*, vol. 44, no. 5, p. L63-L69., 44, L63

383 Wang, R., Lu, Q., Du, A., & Wang, S. 2010a, *Physical
 384 Review Letters*, 104, 175003

385 Wang, R., Lu, Q., Huang, C., & Wang, S. 2010b, *Journal of
 386 Geophysical Research: Space Physics*, 115

387 Wang, R., Yu, X., Wang, Y., Lu, Q., & Lu, S. 2023, *The
 388 Astrophysical Journal*, 947, 78

389 Wang, S., Lu, S., Lu, Q., et al. 2024, *Science Advances*, 10,
 390 eado4639

391 Wu, M., Huang, C., Lu, Q., et al. 2015, *Journal of
 392 Geophysical Research: Space Physics*, 120, 6320

393 Wu, M., Lu, Q., Volwerk, M., et al. 2013, *Journal of
 394 Geophysical Research: Space Physics*, 118, 4804

395 Xing, X., Liu, C., Cao, J., Liu, Y., & Zhao, B. 2024, *The
 396 Astrophysical Journal*, 972, 10

397 Xu, Y., Fu, H., Liu, C., & Wang, T. 2018, The
398 Astrophysical Journal, 853, 11

399 Yamada, M., Kulsrud, R., & Ji, H. 2010, Reviews of
400 modern physics, 82, 603

401 Yang, F., Lu, Q., Zhang, Q., et al. 2025, Geophysical
402 Research Letters, 52, e2024GL114151

403 Yu, Y., Fu, H., Wang, Z., Fu, W., & Cao, J. 2023,
404 Geophysical Research Letters, 50, e2023GL104938

405 Zhang, H., Pu, Z., Cao, X., et al. 2007, Geophysical
406 Research Letters, 34

407 Zhang, T., Lu, Q., Baumjohann, W., et al. 2012, Science,
408 336, 567

409 Zhou, M., Deng, X., Ashour-Abdalla, M., et al. 2013,
410 Journal of Geophysical Research: Space Physics, 118,
411 674, doi: <https://doi.org/10.1029/2012JA018323>